nature communications

Article

https://doi.org/10.1038/s41467-025-58517-8

Percolative sulfide core formation in oxidized planetary bodies

Received: 11 July 2024

Accepted: 25 March 2025

Published online: 04 April 2025

Check for updates

Samuel D. Crossley[1,2,6] ✉, Jacob B. Setera[3], Brendan A. Anzures[4], Kayla Iacovino[4], Wayne P. Buckley[4], Scott A. Eckley[4], Evan W. O'Neal[4], Jessica A. Maisano[5], Justin I. Simon[1] & Kevin Righter[1]

Models of planetary core formation traditionally involve the fractionation of Fe,Ni-metal melts from silicate mantles after extensive silicate melting. However, in planetary bodies that form farther from their central star, where moderately volatile elements are more abundant, high concentrations of oxygen and sulfur stabilize Fe,Ni-sulfides over metals. Here we show that percolative sulfide melt migration can occur in primitive, oxidized mineral assemblages prior to silicate melting in partial melting experiments with meteorites. Complementary experiments with partially molten synthetic sulfides show that fractionation of liquid sulfide from solid residues yields distinct noble metal (Os, Ru, Ir, Pd, and Pt) trace element proportions that match those manifested in the most oxidized meteoritic residues, the brachinites, as well as their complementary basaltic silicate melts. Our experiments provide robust evidence for percolative sulfide melt fractionation in meteorites and indicate that sulfide-dominated cores would be expected in oxidized planetary bodies, including Mars.

Models of planetary core formation differ on the mechanisms and sequence of metal-silicate segregation, often requiring extensive silicate melting to provide migratory pathways for liquid Fe,Ni-metal to sequester into a core (e.g. ref. 1). Recent experiments have demonstrated that metallic melts in large bodies may have been capable of mass migration via percolation at high pressures in Earth's lower mantle, facilitated by deformation from vigorous mantle convection (e.g. ref. 2). Smaller meteorite parent bodies with much lower interior pressures would not facilitate deformation-enhanced percolation of metallic melts during hydrostatic partial melting[3]. However, some meteorite parent bodies were rich in volatile elements (e.g., S and O) with core-forming components that were instead dominated by Fe,Ni-sulfides. The liquids produced from the partial melting of such mineral assemblages may have been capable of percolating through solid silicate media via capillary action (e.g. refs. 3,4). This attribute could have facilitated widescale melt migration and formation of a sulfide-dominated core at lower temperatures and earlier stages of melting in comparison to metallic core formation[5,6]. While models disagree on the efficiency of this process for metallic melts in small bodies, the consensus is that anion-rich melts (i.e., total anion/cation ratio in the melt ≥ 1) are capable of percolative melt migration[3]. Additional factors controlling the percolative potential of melts include: the solidus temperature, S/O content of the melt, FeO content of residual silicates, the initial volume percent of core forming phases, and geometries of residual silicate grains (e.g. refs. 3,5–11), all of which vary between different planetary bodies. The percolative capability of anion-rich (i.e., sulfide-dominated) melt has never been directly assessed under these constraints using actual planetary samples (i.e., meteorites), nor has any conclusive geochemical evidence for this process been positively identified in the meteoritic record.

[1]NASA Johnson Space Center, 2101 NASA Parkway, Houston, TX 77058, USA. [2]Lunar and Planetary Institute, USRA – Houston, 3600 Bay Area Blvd, Houston, TX 77058, USA. [3]CASSMAR, University of Texas at El Paso - Jacobs JETS II Contract, NASA Johnson Space Center, 2101 NASA Parkway, Houston, TX 77058, USA. [4]Jacobs-JETS, Astromaterials Research and Exploration Sciences Division, NASA Johnson Space Center, 2101 NASA Parkway, Houston, TX 77058, USA. [5]Jackson School of Geosciences, The University of Texas, 2275 Speedway Stop C9000, Austin, TX 78712, USA. [6]Present address: Lunar & Planetary Laboratory, University of Arizona 1629 E. University Blvd, P.O. Box 210092 Tucson, AZ 85721, USA. ✉e-mail: crossley@arizona.edu

Previous melt percolation experiments with Fe,Ni-sulfide utilized synthetic mineral assemblages and were heated to temperatures well above the silicate solidus to attain textural equilibrium among olivine grains[3,5–11]. However, immiscible molten sulfide can become entrained within silicate melts, placing limits on the temperature and timing of percolative sulfide melt migration[12]. To accurately determine the potential for percolative sulfide core formation in a planetary body, experimental mineral assemblages must include all phases present at the onset of planetary differentiation. These mineral assemblages must also satisfy requirements for elevated oxygen and sulfur fugacities (log fO_2 ~ IW + 3 and log fS_2 > IT + 2)[13,14] that stabilize Fe,Ni-sulfides over Fe,Ni-metals. All of these mineralogic and geochemical parameters can be met by using equilibrated Rumuruti-type chondrites (RC) as analogues for the precursors of differentiated oxidized bodies[4]. The potential core-forming minerals in RCs include pentlandite $(Fe,Ni)_9S_8$ and pyrrhotite $(Fe,Ni)_{1-x}S$, which begin to melt above 800 °C[15,16], below the silicate solidus temperature for RCs (~1040 °C)[17]. The bulk composition of these sulfide minerals approaches the theoretical anion/cation ratio of 1 that is often required for percolation to occur at low melt fractions in static percolation models[3,4,18]. Identification of newly formed interconnected melt networks in melting experiments would support the hypothesis for mass migration of sulfides in an oxidized parent body, leading to early percolative formation of a sulfide core.

While percolation experiments can demonstrate the physical viability of sulfide core formation, they do not provide direct evidence for its occurrence in the early solar system. However, the geochemical affinities of trace elements can be used to determine the composition of core-forming melts. Noble trace metals (i.e., Os, Ru, Ir, Pd and Pt) are highly siderophile in meteorites containing Fe,Ni-metal (e.g.,), but in oxidized meteorites, they become chalcophile and Fe,Ni-sulfides are the principal mineral hosts of noble metals[4,19]. As sulfides or metals partially melt, noble trace metals partition between coexisting liquid and solid phases in different proportions according to their relative compatibilities, which depends largely upon the compositions of the host mineral and melt (e.g.[20]). The chalcophile behavior of noble metals in oxidized meteorites should therefore leave diagnostic interelement proportions in residual minerals after loss of sulfide melt fractions. However, we found no published trace element distribution coefficients that accurately represent the bulk composition of partially molten RC sulfides at temperatures relevant to percolative sulfide core formation.

In this work, we use a complementary set of partial melting experiments using both meteorites and synthetic geochemical analogues to show that oxidized planetary bodies formed sulfide-dominated cores through percolative migration of molten sulfide prior to silicate melting. This process left diagnostic geochemical signatures among noble metal trace elements in the silicate fractions of oxidized meteorite parent bodies and could also account for observations of the martian core.

Results

Sulfide melt percolation experiments

Whole-rock tomography scans (4.85 μm/voxel resolution) of La Paz Icefield (LAP) 04840, a type R6 chondrite, show clear evidence for melt migration across the experimental temperature range of 900–1020 °C (Fig. 1). In comparison to the unheated sample, multiple sulfide-oxide complexes (SOCs) merged to form mm-scale melt networks due to migration of liquid sulfide by our highest temperature experiment at 1020 °C. Other pre-existing networks were severed into multiple, smaller complexes as melts migrated from their sources. The morphological complexity of SOCs also increased throughout the duration of heating, evident by the increase in surface topography relative to volume (Fig. S1). Detailed dimensional analyses for whole-rock μXCT scans at each temperature step are provided in supplementary materials (text S1).

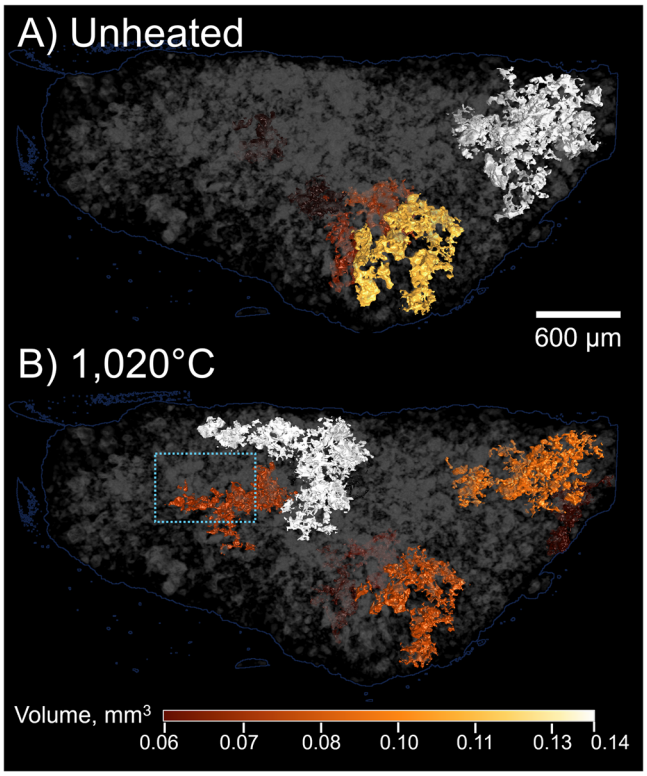

Fig. 1 | Whole-rock 3D tomographic renderings of the largest connected sulfide-oxide complexes (SOCs) in LAP 04840. The unheated sample is rendered in (**A**) vs. after heating to 1020 °C (**B**). The migration of sulfide liquid is evident in the modification of the largest (> 0.06 mm^3) SOC-melt morphologies. The largest SOCs (white) from the unheated sample were severed into smaller networks by melting, while other SOCs and melts merged to form larger networks. Morphological complexity of SOCs increased during heating (Fig. S1), illustrated by dendritic and vermiculated morphologies of SOC-melt networks in **B**. Only the five largest melt networks are rendered in color, for clarity. Silicates are rendered transparent on the black background and smaller SOCs/melts are rendered in semi-transparent grey. Renderings are projected from an identical perspective. The dashed blue box in **B** contains the excised subvolume analyzed in higher-resolution scans (Fig. 2A).

High-resolution tomographic scans (0.7 μm/voxel) of an excised subvolume from the experiment after heating to 1020 °C show that the formation of submicrometer melt veins are responsible for the percolation of molten sulfides among unmelted silicates (Fig. 2). Networks of melt veins are correlated with the formation of vesicles and voids within extant sulfide melt reservoirs and SOCs, indicating that melt veins formed as sulfides melted and drained from their sources. These observations are consistent with the percolative migration of sulfide melts among solid silicate grains via capillary action. Two-dimensional mineralogic and petrographic analysis (text S1) of a polished section confirmed that quenched sulfide melts are homogeneous and permeate unmelted silicate grains by forming submicrometer-thick melt veins (Table S1, Fig. S2). The median dihedral angle of sulfide melts, which is measured as the angle between the surrounding silicate grain boundaries, is 52° (Fig. S3). Static percolation theory predicts that melts with dihedral angles lower than 60° are immediately capable of percolative migration for melt fractions above ~0.1 vol%[18].

Noble metal trace element partitioning experiments

All partial melting experiments with synthetic RC sulfides produced FeNiS liquids with coexisting Ni-rich monosulfide solid solution (MSS) (Fig. 3 and S4, Tables S2-3). Peritectic reaction with FeNiS melt altered residual troilite to Ni-rich MSS, which is consistent with the prediction that pentlandite-troilite assemblages in RCs formed via

https://doi.org/10.1038/s41467-025-58517-8

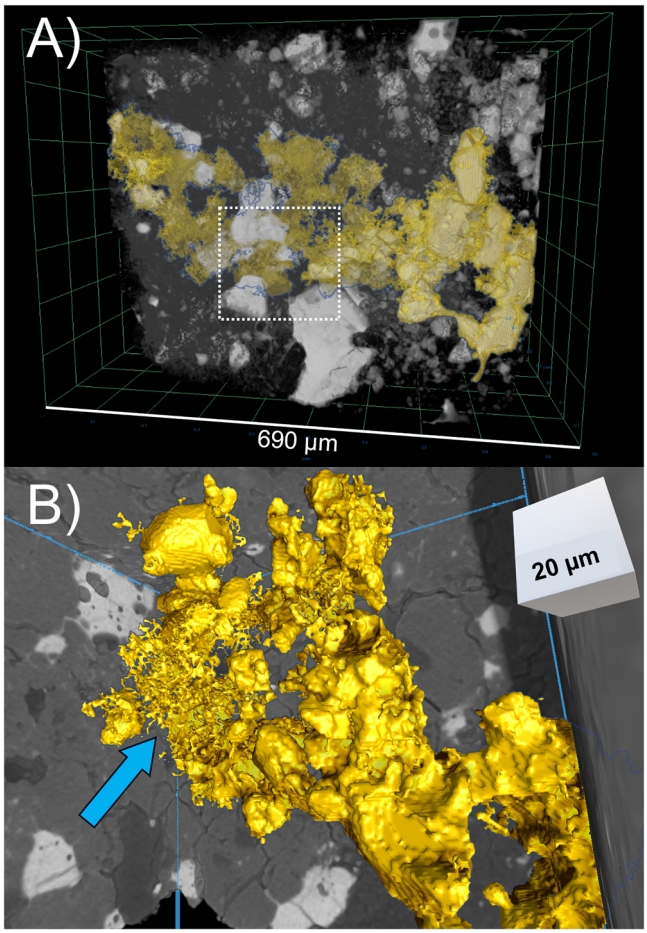

Fig. 2 | High resolution tomographic images of sulfide melts in LAP 04840 after melting at 1020 °C. In **A** silicates (gray) are semi-transparent on a black background and unconnected sulfide-oxide assemblages and separate melt networks are white. The largest interconnected melt network (yellow) spans the entire subvolume with a maximum diameter of at least 690 µm. A closer view of an in situ cutout of the same melt network (dashed box, **B**) shows that submicrometer melt veins (blue arrow) percolated between silicate grains to connect nearby sulfide-oxide complexes.

exsolution from MSS during cooling from metamorphic temperatures (e.g. refs. 21,22). EPMA measurements for MSS in three of four experiments were homogeneous, indicating that equilibrium was attained for major element chemistry. Increasing melt fractions from 900–1020 °C led to greater $D_{Ni}^{MSS\text{-}L}$ due to the peritectic MSS-melt reaction. In the 1060 °C experiment with monomineralic MSS, residual MSS was zoned with Ni concentration increasing from core to rim, potentially indicating only partial equilibration. The 1100 °C experiment yielded homogeneous residual MSS. In all experiments, FeNiS melts quenched to form intergrowths of pentlandite, awaruite, and skeletal MSS dendrites.

Trace element distribution coefficients between MSS and quenched liquid FeNiS across all experimental compositions and temperatures (Table S4-5, Fig. 4) show that Os and Ru are slightly to moderately compatible with MSS ($D^{MSS\text{-}L}$ = 1.3–6.2), Ir is slightly compatible to moderately incompatible ($D^{MSS\text{-}L}$ = 0.25–1.18), and both Pt and Pd are moderately to strongly incompatible ($D^{MSS\text{-}L}$ = 0.001–0.018).

Considering the zonation of Ni in the 1060 °C, it is possible that the 1060 °C MSS experiment reflects the disequilibrium partitioning of noble metals. Disequilibrium in this experiment is likely a result of partial melting slightly above the monomineralic Ni-rich MSS melting point of ~1050 °C[16], slowing the kinetics of noble and base metal diffusion. This potential caveat does not impact interpretations made in this study but should be considered when using our experimental distribution coefficients to model trace element partitioning in future work. As expected for batch melting scenarios, wherein melts remain in contact with residual phases as a closed system, lower melt fraction experiments (i.e., Pn-Tr 900 °C and MSS 1060 °C) are more strongly fractionated with respect to noble metals. In the pentlandite-troilite experiments, the extent of melting, Ni-enrichment of MSS, and $D^{MSS\text{-}L}$ for all noble metals are positively correlated, while interelement fractionation was reduced with progressive melting. This observation is consistent with the prediction that concentrations of sulfide-hosted noble metals are correlated with residual sulfide Ni content during the partial melting of oxidized meteorites[4]. Monomineralic MSS experiments at higher temperatures followed a more typical trend of noble metal fractionation according to their initial compatibilities with MSS at the onset of melting.

Discussion

Our melt percolation experiments with Rumuruti-type chondrites (RC) rapidly generated interconnected sulfide melt networks below silicate melting temperatures. This finding demonstrates that percolative melt migration in oxidized asteroid parent bodies is a viable process within the constraints of meteorite mineral textures and chemistry. The likely factor responsible for the percolation of liquid sulfide is a balance of internal versus external forces between FeNiS liquids and solid silicate mixtures. Previous studies with terrestrial and synthetic mineral analogues have postulated that anion-rich liquid sulfide (anion/cation ≥ 1) may migrate more efficiently through silicate media via capillary action due to the high interfacial energies between liquid sulfides and solid silicates, which exceed the internal cohesive forces (i.e., surface tension) of liquid sulfides[23]. Therefore, during sulfide anatexis in oxidized parent bodies, liquid Fe,Ni-sulfide will maximize its ratio of surface area to volume by wetting grain boundaries of the surrounding silicate matrix until its adhesive and cohesive forces approach equilibrium. In our experiments, the percolative capability of liquid sulfide is evident through the displacement of sulfide melts into the silicate matrix and the formation of interior vesicles, increasing the morphological complexity of sulfides in XCT scans from 900 to 1020 °C. It is unclear if sulfide liquids fully reached cohesive-adhesive equilibrium in our experiments, but the formation of interconnected melt networks demonstrates that sulfide melt migration via percolation is favored during sulfide anatexis.

Given the demonstrated ability of sulfide-rich liquids to percolate among silicate grains in equilibrated meteorites, the remaining limiting factor for widescale percolative migration in meteorite parent bodies may have been the volume of liquid relative to the bulk mineral assemblage. Several previous experimental studies have explored the volumetric percolation threshold for analog mixtures of olivine and Fe-FeS liquids and found that Fe-FeS liquids may form interconnected networks with percolation thresholds between 2-14 vol% (e.g.[6,24]). LAP 04840 contains 0.7 vol% pentlandite and 4.1 vol% pyrrhotite[4], and our tomographic images show ~7 vol% total SOCs, greater than the lowest reported percolation thresholds if extensively melted. The modal abundance of sulfides in RCs can range up to 9.2 vol%[25], which is well above most experimental percolation thresholds for most Fe-Ni-S liquids. However, static percolation theory predicts that partially molten assemblages with dihedral melt angles (i.e., the contact angle between the melt and two adjoining silicate grains) below 60° can mobilize with melt fractions as low as 0.1 vol%[18]. The average dihedral angle measured in our percolation experiments is 52°, suggesting that melts should be immediately capable of migration, consistent with our tomographic observations. These predictions are further supported by recent computational fluid dynamics models for Fe-S melt permeability, which suggest that anion-rich melts like those produced in our experiments should be capable of percolation until near complete exhaustion of sulfide melts in the source[10]. According to these

https://doi.org/10.1038/s41467-025-58517-8

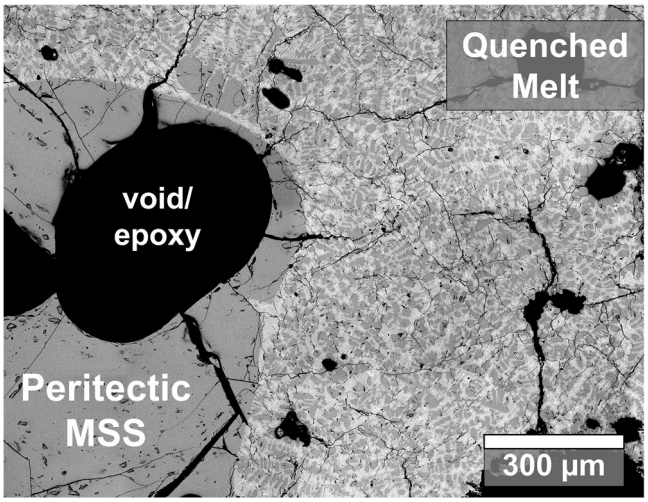

Fig. 3 | Back scattered electron (BSE) image from the noble metal partitioning experiment with pentlandite and troilite at 1020 °C. Peritectic reaction of the FeNiS melt with troilite produced Ni-rich (6.9 wt%) monosulfide solid solution. Pentlandite-rich FeNiS melts quenched to form intergrowths of pentlandite, awaruite metal, and dendrites of Ni-rich MSS with the same composition as peritectic crystals.

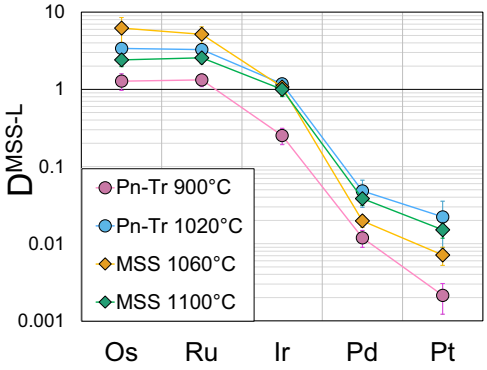

Fig. 4 | Molar distribution coefficients for noble metals in partial melting experiments arranged by decreasing compatibility with MSS. The relative affinities of noble metals are maintained through progressive melting of pentlandite-troilite assemblages (circles), even after loss of pentlandite melt and melting of monomineralic MSS (diamonds). The degree of fractionation corresponds with batch melting, where the experiments with the smallest melt fractions are the most fractionated. Pentlandite-troilite experiments show that noble metal fractionation is further complicated by the formation of peritectic MSS, which hosts greater proportions of all noble metals as melting progresses. Error bars represent 2 standard errors. Data is reported in Table S4-5.

numerical simulations, even a seemingly negligible fraction of molten sulfide generated at temperatures below 900 °C may be capable of triggering percolative sulfide melt migration in oxidized asteroid parent bodies.

As demonstrated in our melt percolation experiments, FeNiS liquids can migrate through silicate media as temperatures approach 1020 °C. As a result, we used the trace element distribution coefficients from our 1020 °C experiments with pentlandite-troilite mixtures as a comparison to interelement ratios of noble metals in the most oxidized primitive achondrite meteorites (i.e., brachinites). Interelement ratios of noble metals in our experiments provide a test to distinguish between Fe,Ni-sulfide versus Fe,Ni-metal fractionation in oxidized primitive meteorites (e.g.[26]). In our experiments, the relative affinities of noble metals between MSS and liquid FeNiS are consistent with interelement ratios for bulk measurements of oxidized brachinites (i.e., $D^{MSS\text{-}L}$ = Os,Ru >Ir > >Pd,Pt). Additionally, the degree of interelement fractionation in our experiments matches some reported measurements for individual sulfide measurements in oxidized brachinites[26]. However, noble metals in our experiments are more strongly fractionated than bulk measurements of brachinites (e.g.[26–28]). A simple explanation for the differing extent of noble metal fractionation between our experiments and bulk meteorite measurements is that the brachinites continued melting beyond 1020 °C. This is evident from the loss of a silicate partial melt component and mineral closure temperatures from brachinites in excess of 1020 °C (e.g.[26,29]). In a batch melting scenario for sulfides, an increasing melt volume reduces the interelement fractionation of noble metals between residual MSS and melt, bringing interelement ratios back toward unity. Our high-temperature, monomineralic MSS experiments show that the compatibilities of noble metals do not change even if pentlandite-rich melt is removed from the system, so we modeled continued batch melting from our experimental melt fraction produced at 1020 °C (F = 0.87 ± 0.03) and found that 89–94 ± 3% partial melting of pentlandite-troilite mixtures can reproduce the entire range of reported noble metal interelement ratios in oxidized brachinites (Fig. 5, Table S6). The peritectic reaction between troilite and FeNiS melt results in increasing $D^{MSS\text{-}L}$ for both Ni and noble metals, which reflects the elevated noble metal contents of brachinite sulfides alongside the presence of pentlandite exsolution lamellae in brachinite troilite[26].

The oxidized brachinites are not the only meteorites with anomalous noble metal proportions that can be reproduced by our experimental results. Oligoclase-rich achondrites, i.e., Graves Nunatuk (GRA) 06128/9, possess similar interelement proportions among noble metals and are regarded as the complementary crustal silicate melt fractions for brachinite residues[27]. As we have demonstrated, sulfide melts can percolate prior to silicate melting, which leads to interelement fractionation of noble metals prior to silicate melting. We also show that the first partial melts of sulfides are enriched in incompatible noble metals (i.e., Ir, Pd, and Pt), so these melts must have already migrated away from their sources prior to silicate melting in the brachinite parent body. Otherwise, initial sulfide melts would have become entrapped within molten silicates, resulting in incompatible noble metal enrichment in the crust.

We propose that oxidized differentiation in the brachinite parent body included three stages of melting (Fig. 6). In the first stage, early percolative migration of FeNiS liquid left residual Ni-rich MSS in the brachinite precursor that was depleted in incompatible noble metals. As temperatures reached the silicate solidus at ~1050 °C[17], the second stage of oxidized differentiation began through anatectic melting of both residual Ni-rich MSS and silicates. Experimental work has shown that µm to mm-scale MSS melt droplets become entrained in viscous crustal silicate melts formed during partial melting of peridotite assemblages like those of RCs[12]. As silicate melting progressed and formed an interconnected melt network, the third stage of oxidized differentiation began, wherein silicate melts buoyantly ascended to form the oligoclase-dominated crust, carrying a portion of molten MSS and establishing similar noble metal proportions in both brachinite residues and crustal melts.

The decay of short-lived radionuclides like ^{26}Al, and possibly ^{60}Fe, are the primary candidates for the heat source that drove the internal differentiation of planetesimals (e.g.[30]). Numerical simulations of differentiation suggest that internal temperatures exceeding the sulfide solidus could be reached via short-lived radionuclide decay for bodies larger than 20 km if they accreted within ~3 Ma of the Solar System formation[31]. These conditions are satisfied by primitive achondrites and chondritic meteorites from the inner Solar System, which accreted in the first 1.0–2.2 Ma of the Solar System[32] and whose parent body diameters ranged from ~50 to 150 km (e.g.[33,34]). In our experiments, the observed percolative migration of molten sulfide reflects models for

https://doi.org/10.1038/s41467-025-58517-8

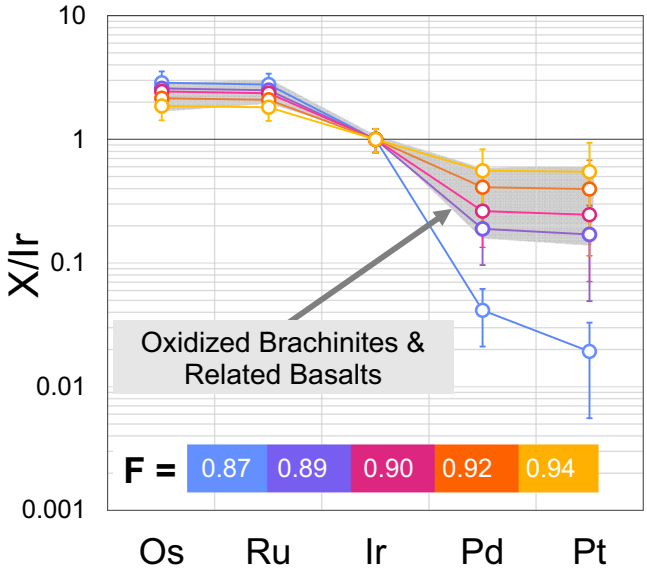

Fig. 5 | Interelement ratios for noble metals in partially molten sulfides from experiments and meteorites. X is a given noble metal normalized to Ir. Ratios and propagated uncertainties (2 standard errors) are from D^{MSS-L} in the 1020 °C experiment and batch melting models (Tables S5-S6). For meteorites, ratios are taken from CI-normalized bulk concentrations[26–28]. F = melt fraction. The 1020 °C pentlandite-troilite melting experiment yielded 87% melting of sulfides (blue), reproducing the relative compatibilities of noble metals in oxidized brachinites and complementary oligoclase-rich basalts (grey field). Model results for continued batch melting (89-94% ±3%) reproduce the full range of interelement ratios in brachinites and related basalts. These ratios cannot be reproduced through simple solid-liquid Fe,Ni-metal partitioning. The similar noble metal proportions for restites (i.e., brachinites) and their basaltic melt fractions implies that an initial Pd,Pt-enriched sulfide liquid had already fractionated prior to silicate melting, most likely leading to core formation through percolative melt migration. CI normalization is from[78].

percolative core formation occurring within the first million years of accretion in small bodies. Silicate anatectic melting and extrusion can occur subsequently within another 0.5–2 Ma, dependent upon parent body size and accretion rate[31]. This period between the melting of sulfides and silicates is sufficient for molten sulfide to percolate to the center of a ~100 km body and form a core, assuming reasonable melt flow velocities of 1-100 m/yr[8]. Such rates of migration are slow enough that noble metal equilibration between melts and residual sulfides would still effectively resemble a batch melting scenario[20].

These findings provide the first meteorite-based evidence for the occurrence of percolative sulfide melt migration in the early Solar System. Sulfide melt percolation probably initiated core formation in small, oxidized bodies, but the results of our experiments cannot directly assess if melts specifically sequestered at the center of the brachinite parent body to form a discrete core. However, in the context of the broader understanding that many so-called "primitive" bodies contained partially differentiated interiors with magnetic dynamos[35], it is reasonable to conclude that oxidized asteroid parent bodies like those of RCs and brachinites, lacking substantial amounts of Fe,Ni-metal, formed sulfide cores through percolative melt migration. Presumably, the displaced sulfide melts were sequestered into a core through buoyant displacement of less dense silicate grains/liquids at the center of the parent body. Further experiments are needed to constrain the crystallization sequence of an oxidized FeNiS core, but we can make predictions using Fe-Ni-S phase equilibria (e.g. refs. 36,37) and computational models for pure troilite core formation[38]. For the melt compositions generated in our experiments between at 900 and 1020 °C, a small fraction (~1 vol% of the core) of Ni-rich metal (45–60 at% Ni) may be the first component to crystallize during cooling[4]. Due to its high density, the metallic fraction would subsequently sink to the center of the core. Fractional crystallization of Ni-rich metal would elevate the FeS content of the liquid toward the pentlandite-MSS stability field. Subsequent crystallization would likely follow models for pure troilite cores, in which floatation of crystallizing MSS in a dense FeNiS liquid led to the formation of a solid MSS layer at the core-mantle boundary[38]. This layer could impede further draining of sulfide melts into the core, resulting in the accumulation of entrapped sulfide melts at the base of the mantle. Core crystallization would then progress inward with the melt becoming progressively Ni-rich and S-poor. This progression would yield a rim-to-core profile of MSS characterized by increasing Ni content, followed by pentlandite, and possibly a small, Ni-rich metallic inner core (Fig. 6). Slow cooling of the sulfide core would then exsolve additional pentlandite from Ni-rich MSS to form troilite. While sulfide-dominated meteorites akin to metallic iron meteorites have yet to be confirmed in the meteorite record, ungrouped Ni-rich iron meteorites like Oktibbeha County[39] may represent the innermost core materials formed during oxidized differentiation[4].

Rumuruti-type chondrites are the most oxidized and sulfur-rich primitive meteorites from the inner Solar System, though many carbonaceous chondrites formed in similarly volatile-rich regions of the protoplanetary disk. If carbonaceous chondrites represent outer Solar System materials, as it is often assumed[40,41], then percolative sulfide melt migration may have been a more prevalent mode of core formation beyond the snow line, where volatile elements condensed into ices. For example, if melting occurred in the interior of the carbonaceous Yamato-type chondrite (CY) parent body, the high modal abundance of sulfides (10–30 vol% FeS)[42] would have readily facilitated the formation of interconnected melt networks. Evidence for this may be preserved in the paleomagnetic signatures of sulfides in CY chondrites, as many chondritic parent bodies, including those of R chondrites, record paleomagnetic signatures that could indicate partially differentiated interiors[35,43,44]. Likewise, the optically opaque assemblages of the carbonaceous Karoonda-type chondrites (CK), the most oxidized of all known meteorites (log fO_2 = IW + 7), are dominated by magnetite, pentlandite, pyrrhotite, and pyrite[45]. If the interior of the CK chondrite parent body or a mineralogic analogue had partially melted, according to predictions from static percolation theory[18], even a few vol% of S-rich melt could have facilitated percolative melt migration and core formation. Melt percolation experiments of CK meteorites, similar to those reported here, would provide more direct evidence for the possibility of sulfide melt percolation in carbonaceous chondrites.

Evidence for sulfide melt percolation may also be preserved in stony-iron meteorites like mesosiderites and pallasites. Textural analyses of stony-irons show interstitial troilite among silicate clasts, which are surrounded by Fe,Ni-metal matrices. While some sulfides are probably derived from the metallic source, recent textural investigations suggest that a fraction of sulfides and metals are endogenous to restitic silicate clasts[46]. If the precursors of silicate clasts in pallasites and/or mesosiderites were partially molten and laced with sulfide melt networks, the consequences for their mechanical strengths may explain the dearth of mantle materials in both the meteorite record and the asteroid belt. Although additional experiments are needed to quantify the effects of interstitial sulfide melts on the mechanical strength of mantle materials during impact, some inferences can be drawn from studies of the terrestrial mantle and metallurgy. The cohesive strengths of mantle mineral assemblages are reduced by the presence of partial melts[47]. Similarly, the cohesive strengths of oxidized parent body mantles should be reduced by the presence of interstitial sulfide melt networks, which would bear similar cohesive energies to mechanically weak, crystalline Fe,Ni-sulfides[48]. Thus, during catastrophic impact, mantles that were permeated by sulfide melt networks would have been more readily disaggregated and only

https://doi.org/10.1038/s41467-025-58517-8

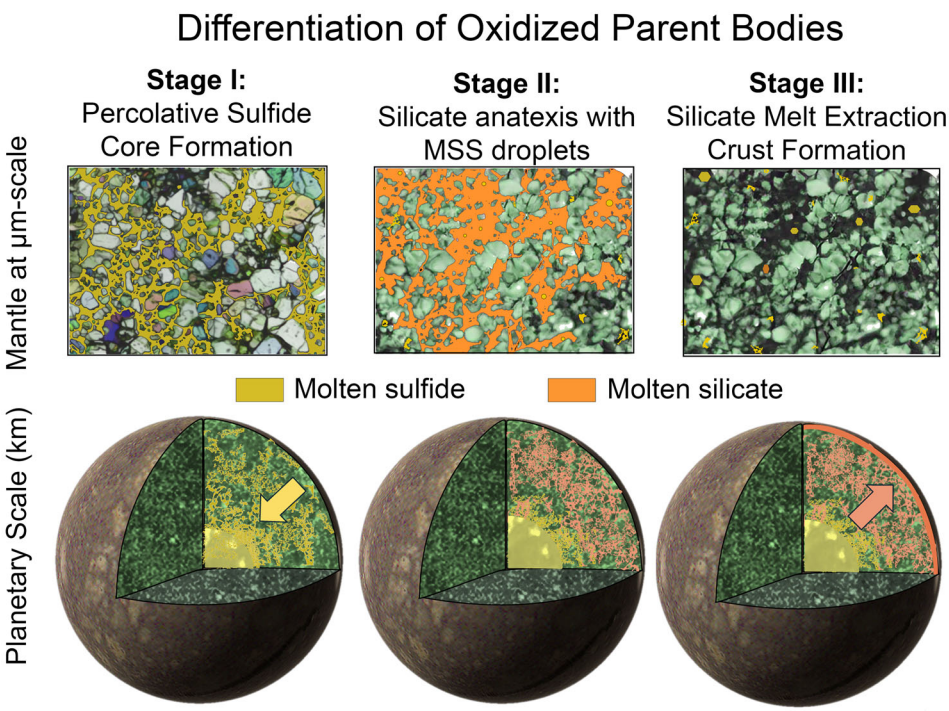

Fig. 6 | Schematic of the sequence of planetary differentiation in oxidized (log fO_2 > IW-1) parent bodies. Stage I: in oxidized bodies, core-forming assemblages were dominated by Fe,Ni-sulfides, which began melting near 800 °C. The initial sulfide liquids percolated toward the center of the body to form an Fe,Ni-sulfide core. Stage II: after fractionation of initial sulfide liquid, silicates began to melt anatectically, entraining a small fraction of immiscible MSS melt droplets. Stage III: Molten silicates and immiscible MSS melt droplets buoyantly ascended to form the crust, leaving the mantles of oxidized parent bodies depleted in heat-producing ^{26}Al and leading to the formation of mantle restites like the brachinites. The crystallization sequence of the sulfide core is not well-constrained (see text), but may have led to the formation of a small Ni-rich metallic inner core with a large outer core composed of monosulfide solid solution that crystallized inward with progressively Ni-rich and and S-poor melts crystallizing last to form pentlandite at the inner-outer core boundary. Ni-rich MSS would subsequently exsolve to troilite and pentlandite during cooling.

preserved in instances where they were quickly immersed in a mechanically resilient matrix, such as liquid Fe,Ni-metal.

Application of our findings to larger planetary bodies with greater internal pressures must account for the effects of pressure on the permeability of sulfide melts. There is some disagreement among numerical models and partial melting experiments regarding the influence of pressure on the permeability of sulfide melts in silicate matrices from 1 atm to 4 GPa[2,3,5–10,49]. Additional work is needed to quantify the relationship between pressure and permeability over this range, but the majority of published findings agree that the anion/cation ratios of FeNiS melts are the primary controls on percolative ability[3,5–7,10]. In some experiments at higher pressures, the wettability of Fe-sulfide melt has been shown to increase at pressures of ~4–20 GPa[49], which includes pressures analogous to the martian core-mantle boundary. The constraints currently available in literature suggest that anion-rich melts, like those in our study, are similarly capable of percolative melt migration at pressures relevant to the martian interior.

Regarding the relevance of martian mantle redox state, oxybarometry from martian meteorites and in situ analyses of unaltered surficial basalts suggest that their mantle source fO_2 ranges from ~IW to IW + 3.5[50], coincident with the redox state of many R chondrites. It is unclear how fO_2 may have evolved in the martian mantle since core-mantle differentiation, but the most reducing estimates for fO_2 during martian core formation are between IW-1 and IW-1.5[51–53], similar to the fO_2 range for oxidized brachinites[26]. It follows that the mineralogy of core-forming phases may have been similarly biased toward sulfides and oxides, in lieu of Fe,Ni-metals. This is consistent with the high S content (> 20 wt%) of the martian core interpreted from seismic measurements[54,55]. Recent studies argue that such high S contents defy cosmochemical constraints from S-rich chondrites (e.g.[54–56]), although such assertions are inconsistent with the existence of RCs, whose core-forming minerals contain 33–36 wt% S (e.g., [4]) and otherwise possess silicate mineralogies akin to ordinary chondrites that formed at high fO_2[57]. Experimentally measured acoustic properties of S-rich (~32–36 wt% S) FeNiS liquid at pressures and temperatures relevant to the martian core yield core size and density profiles consistent with measurements from the Insight seismometer[58], lending further evidence to support a sulfide-dominated martian core. Notably, the interpreted S content from Insight[54] may have underestimated S content of the martian core due to models based on the elastic properties of FeS liquid, which differ markedly from acoustic velocity measurements of liquid FeNiS at martian core conditions[58].

Sulfide-dominated core formation for Mars may also be favored by trace element geochemistry. The estimated noble metal contents of the martian mantle, inferred from crustal martian meteorites (Ref. 59 and references therein), preserve modest Ir and Pt depletions that can be reproduced with our sulfide partial melting experiments. Otherwise, noble metal proportions for the martian mantle require fractionation of S-undersaturated liquid metal[59], which is inconsistent with the high S contents inferred from seismic observations.

Further disagreement on the timing of martian core formation and late accretion comes from the interpretation of Hf-W isotopic ages for martian meteorites, though these issues can also be mitigated if differentiation processes are considered under more oxidizing conditions. Ages derived from Hf-W isotopes may indicate that Mars either rapidly formed a metallic core[60] or a significant portion (0.25%) of martian W was accreted after core formation[61]. However, if martian mantle fO_2 was near IW during differentiation, then it was also coincident with the W-WO_2 oxidation buffer[62]. Under these fO_2 conditions,

the assumed siderophile affinity of tungsten in Hf-W core formation modeling is not applicable as it partitions equivalently among Fe,Ni-sulfides, Fe-oxides, and silicates[4]. Therefore, percolative formation of a sulfide-dominated core would have minimally fractionated W from the silicate assemblage. Instead, with an initial Hf/W ratio of ~4 in the primitive martian mantle[63], the Hf-W system would have been more strongly controlled by the partial melting of silicates as Hf partitioned into primary crustal melts. This petrogenetic sequence would lead to Hf/W ratios between 50-100, satisfying isotopic anomalies in crustal martian meteorites without the need for rapid metallic core formation or late accretion[64,65].

Thus, if percolative sulfide melt migration was the principal contributor to martian core formation at moderately oxidizing conditions (> IW-1.5), then a large, low-density, S-rich core could have rapidly formed, followed by silicate partial melting and the formation of a global silicate magma ocean, consistent with known cosmochemical, chronological, and seismic constraints for Mars.

Methods

Experimental methods: melt percolation

All partial melting experiments in this study were conducted in the Experimental Petrology Laboratory at Astromaterials Exploration and Research Science Division (ARES), NASA JSC. To assess the potential for percolative melt migration in meteorite parent bodies with equilibrated mineralogies and textures, we conducted a set of iterative partial melting experiments in evacuated SiO_2 glass tubes with a 200 mg chip of R6 chondrite La Paz Icefield (LAP) 04840 at temperature steps of 900 and 1020 °C. These temperatures isolate melting of sulfides (i.e., pentlandite and troilite) prior to silicate anatexis in RCs (~ 1050 °C)[17]. LAP 04840 was selected for its high petrologic type (R6)[66] that most closely approaches textural equilibrium during anatexis. Gas fugacities were not directly imposed in this experiment. Instead, the fO_2 and fS_2 of the system are buffered by the bulk mineralogy of the sample, which was sealed under vacuum to prevent S volatilization through reaction with atmospheric gases. LAP 04840 equilibrated at log fO_2 = iron-wustite (IW) + 3 and log fS_2 = iron-troilite (IT) + 2[13]. The quenched sulfide melts from our experiments approximate the composition of initial sulfide mixtures, indicating that chemical equilibrium was maintained with the transient experimental gas fugacities in the assembly. Silica glass tubes were placed vertically in a box furnace and heated for 48 h at each temperature step. At the end of each temperature step, the tubes were submerged in ice water to rapidly quench experiments and preserve the textures of liquid sulfides with minimal annealing.

Prior to heating and after each temperature step, the meteorite chip and silica tube were scanned in situ using micrometer-scale X-ray computed tomography (μXCT, voxel resolution = 4.85 μm) at ARES NASA JSC to observe the mobilization of sulfide liquids. After the final whole-rock scan, the sample was extracted, mounted in epoxy, bisected using a diamond wire saw, and polished for two-dimensional petrographic analysis. A final high-resolution scan (voxel resolution = 0.7 μm) of an excised subvolume of the polished 1020 °C experiment was collected at the University of Texas High-Resolution X-ray Computed Tomography Facility (UTCT) in Austin, TX. The subvolume was cut from the sample using a diamond wire saw and analyzed as a 1x1x4-mm matchstick.

Experimental methods: noble metal trace element partitioning

Trace element partitioning was investigated by partially melting synthetic RC sulfide mixtures of pentlandite-troilite (Pn-Tr) and monosulfide solid solution (MSS, 8 wt% Ni) in evacuated SiO_2 tubes at 900, 1020, 1060, and 1100 °C. Noble metal trace elements (Os, Ir, Ru, Pt, and Pd) were doped at 5 ppm in Pn-Tr experiments and at 10 ppm for monomineralic MSS. Starting sulfides were synthesized by mixing elemental Fe, Ni, and S reagent powders at proportions equivalent to reported compositions of equilibrated type 5/6 RC sulfides[4]. Noble metal trace elements were introduced to mixtures by doping S powders with AAS standard solutions, then allowing the solution mixture to evaporate at 60 °C in a drying oven for ~3 h to prevent oxidation of Fe and Ni metal powders[67]. Once dried, the Fe, Ni, and doped S powders were ground in an agate mortar and pestle until homogeneous. Each sulfide mineral mixture was sealed in a separate silica tube and placed into a box furnace for synthesis. Troilite and MSS were synthesized via chemical vapor transport at 800 °C for 48 h[67], while pentlandite was melted at 1100 °C for 1 h, then sintered at 700 °C for 24 h[68]. For the Pn-Tr experiments, only pentlandite was doped with trace elements, as equilibrated RC pentlandite is the main carrier of noble metals[4]. After synthesis of stoichiometric troilite and doped pentlandite, 1:1 mixtures were homogenized in an agate mortar and pestle and sealed in an evacuated SiO_2 tube, then brought to temperature in a box furnace at approximately 2 °C/s. Experiments were held at peak temperature for 48 h, which allows for noble metal equilibration during partial melting of Fe,Ni-sulfides[20]. Partial melting in the evacuated experimental assemblies eliminates partitioning uncertainties related to porosity, as melts fill in pore spaces between residual sulfides. We did not directly impose fO_2 in these experiments, but our synthetic sulfide assemblages reflect those of RC meteorites that equilibrated between IW-1 to IW + 3, so the experimental partitioning behaviors of trace elements between solid and liquid sulfide are representative of sulfide partial melting in comparatively oxidized systems. At the end of each experimental run, glass assemblies were quenched in water and the experiments were extracted, mounted in epoxy, and polished with Al_2O_3 powder and ethanol for elemental analyses.

Analytical methods

In all experiments, mineralogy and petrography were first investigated using reflected light microscopy, followed by backscattered electron (BSE) imaging and semi-quantitative elemental composition via electron X-ray dispersive spectroscopy using a Phenom XL benchtop scanning electron microscope at the Lunar and Planetary Institute SEM Facility. Dihedral angles of sulfide melts were measured using the Angle Measurement tool on ImageJ software with BSE images collected with a Hitachi TM 4000+ tabletop SEM at the University of Arizona's Lunar and Planetary Laboratory. Quantitative major element compositions of sulfides and melts were measured via electron probe microanalysis (EPMA) using the JEOL 8530 F at ARES, NASA JSC. Analyses were collected with beam conditions at 15 kV and 20 nA using a 1 μm spot size. EPMA measurements were calibrated using analytical standards for Si (Si-metal), Mg (MgO), Al (corundum), S (troilite), Ca (diopside), Ti (rutile), Cr (chromite), Mo (Mo-metal), Fe (troilite), Ni (Ni-metal), and Mn (Rhodonite). This suite of elements allowed us to assess potential melt contamination from oxides and silicates. Analytical uncertainty for EPMA measurements were less than 0.7% RSD for all elements.

In situ trace element concentrations were measured via laser ablation inductively-coupled plasma mass spectrometry (LA-ICP-MS) using a Thermo-Scientific Element-XR coupled to a Photon Machines 193 nm excimer laser ablation system at the Center for Isotope Cosmochemistry and Geochronology facility at ARES NASA JSC. Prior to the sessions, the gas flows and ICP-MS settings were tuned to limit fractionation and oxide production by ablating a raster on NIST 612 glass and obtaining Th/U = 0.97 and Th.O/Th% = 0.12. To limit matrix-dependent down-hole fractionation effects from typical ablation pit aspect ratios, LA-ICP-MS analyses for standards and unknowns were conducted as raster patterns (150 μm in length for standards, and ~500-2000 μm in length for unknowns) moving at 3 μm/s, using a 10 Hz shot frequency, and with a pre-ablation "cleaning" scan for each location of interest. Spot sizes were optimized for the available surface area of the synthesized sulfides and standard analyses were conducted at the same conditions for spot-size specific data processing. The variable

demagnification optics of the laser ablation system were used to achieve fluences of ~2.72 J/cm^2 and ~2.91 J/cm^2 (using a 7 mJ setpoint) at the sample surface for the 240 μm and 210 μm spot sizes, respectively. The 10x10X demagnification setting was also used for the 130 μm spot sizes, producing a fluence of ~3.25 J/cm^2 at the sample surface, while the standard 16x16X demagnification setting was used to produce a fluence of ~3.00 J/cm2 at the sample surface for the 155 μm spot size.

A total of 23 analytes were collected, while dwell times ranged from 0.01 ms (trace elements) to 0.05 ms (major elements), with a total sweep of the mass range taking ~0.67 s. Specific to this study, the following masses were collected in low resolution: ^{57}Fe, ^{99}Ru, ^{101}Ru, ^{105}Pd, ^{108}Pd, ^{189}Os, ^{193}Ir, ^{195}Pt. Each raster pattern was followed by an ~90 s washout and a subsequent 20 s gas blank measurement before the next pattern. We regularly analyzed iron meteorites as primary calibration materials (Hoba and Filomena)[69], while also regularly analyzing an in-house synthetic sulfide to ensure accuracy. Data processing was completed using Iolite's "3D Trace Elements" reduction scheme[70] with ^{57}Fe used as an internal standard and limits of detection were calculated using the method of[71].

Trace element abundances were normalized to Fe wt% measured via EPMA. Even rapidly quenched sulfide melts produce complex intergrowths of multiple mineral phases (i.e., pentlandite-MSS-awaruite), so we calculated Fe content of ablation lines for quenched melts using EPMA measurements of individual quench phases weighted by their modal abundance within the ablated surface area. Modal mineralogy of quenched melts was determined using image segmentation and classification algorithms in the XMapTools software, which utilizes elemental EDS maps and user-defined regions-of-interests to iteratively determine pixel classification parameters for each mineral phase, then applies the final classification parameters to all pixels in the image[72,73]. Consequently, the standard deviations of elemental concentrations in an ablation line are more representative of quenched melt heterogeneity than analytical uncertainty. To account for phase heterogeneity, we took weighted means using the standard deviations of each ablation line. An overdispersion factor was applied to the weighted means where the chi-square test p-value was less than 0.05 (i.e., 95% confidence interval). The overdispersion factor was calculated as in[74]:

$$\sigma_2 = \sigma_1 \cdot \sqrt{\text{MSWD}} \quad (1)$$

where σ_2 is the standard deviation of the weighted mean calculated with overdispersion, σ_1 is the original calculated standard deviation of the weighted mean without overdispersion, and MSWD is the mean square weighted deviation. Corrected trace element concentrations are summarized in Table S4.

X-Ray Computed Micro-Tomography

Whole-rock X-ray computed tomography (XCT) imaging of the melt percolation experiments was performed at the X-ray Fluorescence and Computed Tomography (X-FaCT) Laboratory at ARES NASA JSC using a Nikon XT H 320 scanner equipped with a 180 kV nano-focus tungsten transmission target (spot size ~1 μm) and a 2000 x 2000-pixel Perkin Elmer flat-panel detector. All scans (pre- and post-heating) were performed using the same conditions. X-ray tube energy was set at 95 kV and 3.0 W with 3141 projections through a 360° rotation using 8 frames averaged per projection at 1.0 s exposure per frame. X-rays were prefiltered using 0.5 mm of Al. Projection images were reconstructed into a 3D volume using Nikon's CTPro3D (v. 5.4) proprietary software, which also implements beam hardening and noise correction functions. Reconstructed voxel sizes (i.e., a pixel with a third dimension) are 4.85 μm/voxel edge.

The reconstructed 3D volume, which is output as a contiguous series of 2D (X and Y) 16-bit grayscale images (slices) oriented orthogonally to the scan rotation axis (Z), comprises a grid of cubic voxels that map differences in effective X-ray attenuation. Each voxel is assigned a value (CT number; CT#) reflecting the effective X-ray attenuation of the material within that voxel. X-ray attenuation is a function of a material's mean atomic number, mean density, and X-ray energy. Voxels with a greater effective X-ray attenuation (i.e., higher-z and higher density) are assigned higher CT#s, which are visualized with brighter gray values[75].

To image the submicrometer melt vein observed in the BSE images of the final 1020 °C melt percolation experiment, we excised a "matchstick" subsection from the interior of the sample (1x1x4 mm) using a diamond wire saw at ARES NASA JSC. The sample was then taken to UTCT in Austin, TX for high-resolution scans using a Zeiss Xradia 620 Versa scanner. X-ray tube energy was set at 80 kV and 10 W with 2401 projections at 5.0 s exposure time. Beam hardening and noise correction functions were applied to remove analytical artifacts. Scans produced 954 slices with 0.7 μm voxel size.

Scans of experiments were rendered in 3D using ORS Dragonfly software (Comet™ Technology). Sulfides were segmented from other mineral phases using global greyscale thresholds for voxel brightness (i.e., CT#). Due to their high Fe content and densities, sulfides and oxides have the highest X-ray attenuation among phases in experiments and therefore comprise the brightest voxels with the highest CT#s. The segmentation threshold distinguishing sulfide-oxides from the next most attenuating phase, FeO-rich olivine, was set as half the difference between their respective average CT#s to mitigate misclassification of sulfide-oxides with "smeared" grain boundaries where CT#s are averaged between sulfides and neighboring mineral grains. We estimate that this could result in the loss of up to 37% of total sulfide-oxide volume during voxel segmentation (i.e., sulfides and melts veins that fall below voxel resolution, as well as the volume at grain boundaries lost to voxel smearing), so the reported volumes of sulfides should be considered lower limits. The interconnectivity of sulfides was determined using the Connected Components function in ORS Dragonfly software, which further segments sulfides into separate ROIs by nearest neighbor classification. To provide the most conservative estimates for interconnectivity, we selected face-oriented classification, which only considers two voxels to be connected if their faces are in contact. Given that some sulfides and melt veins fall below voxel resolution and are averaged with lower CT# phases, this also likely undersamples the connectivity of sulfide voxels. Thus, the extent of interconnectivity for sulfide melts in our experiments should also be taken as lower limits.

The evolution of morphologic complexity for sulfides and melts in our experiments was quantified following methods in[76]. This approach calculates a convolution index (CVI) using a ratio of the surface area of a connected component (i.e., SOC or melt network) to the surface area for a sphere of equivalent volume. Higher CVIs therefore represent greater morphological complexity of objects at a given volume (Fig. S1). The evolution of morphological complexity for the overall population of SOCs and melts were assessed using linear regressions through CVI calculations and equivalent sphere diameters at each temperature step. Greater slopes for linear regressions indicate the increasing morphological complexity of the population. Detailed dimensional analyses for experiments are provided in the appendix (Text S1, Fig. S1).

Partial melting models

The fraction of melting in the noble metal partitioning experiment at 1020 °C could not be directly measured due to the heterogeneous distribution of MSS grains and melt in polished sections. Instead, the extent of melting was calculated from noble metal distribution using the batch melting equation,

$$C_l/C_0 = 1/(D(1-F)+F) \quad (2)$$

where C_l is the noble metal concentration in the liquid measured with LA-ICP-MS, C_o is the original bulk concentration, D is the distribution coefficient calculated as the ratio of noble metal concentration in MSS to concentration in liquid (i.e., $D^{MSS\text{-}L}$), and F is the melt fraction. Our experimental results provided data for all other variables and were used to solve for F for each noble metal.

Calculated melt fractions for Os, Ru, and Pd agreed within their uncertainties propagated from LA-ICP-MS measurements. Calculations for Ir and Pt yielded calculated melt fractions that were inconsistent with petrographic observations and/or yielded improper fractions (F = 0.63–2.08). Both Ir and Pt are known to form selective complexes with S and semimetals during melting (e.g. ref. 77), which further complicates their partitioning behaviors. This factor likely contributes to the lower $D^{MSS\text{-}L}$ for Ir and Pt in experiments and natural samples but compromises their utility in calculating melt fractions during batch melting. Considering the agreement between F calculations using the other noble metals, we disregard the calculated melt fractions from Ir and Pt in favor of concordant values for Os, Ru, and Pd in the 1020 °C experiment.

The batch melting equation is suitable for calculating F in these closed-system equilibrium experiments, although a natural system is unlikely to be truly closed, and the peritectic reactions forming Ni-rich MSS would further obfuscate equilibrium trace element partitioning models. Given the aforementioned petrologic and geochemical complications and the near complete melting of sulfides across our experiments, further melting in these systems was simulated using weighted averages of experimental trace element ratios (e.g., $D_{Os}^{MSS\text{-}L}/D_{Ir}^{MSS\text{-}L}$) and initial interelement bulk ratios (i.e., ratios of 1) between experimental melt fractions ($F \gtrsim 0.9$) and complete melting (F = 1). This approach mitigates the above complications and allows for the comparison of interelement ratios with those in CI-normalized bulk measurements of meteorites, as partial melting in both systems begin with noble metal interelement ratios of approximately 1. With progressive batch melting in these models, the initial interelement fractionation of noble metals decreases back toward unity as the system approaches complete melting of sulfides.

Application of Equilibrium Batch Melting Experiments to Meteorite Interpretations

Noble metal interelement ratios were compared to those reported for bulk meteorite assemblages, rather than individual sulfide grains. This approach was selected because noble metal equilibration between isolated sulfide/metal melts, which are separated by residual silicates, is inefficient (e.g.[19]), resulting in noble metal heterogeneity for any SOCs or melts that were disconnected from other melt networks. Whole-rock noble metal measurements of meteorites represent diluted averages of sulfides, which are the primary mineral hosts of noble metals in oxidized meteorites[4,27]. Therefore, interelement ratios from bulk measurements provide the most direct comparison with our equilibrium batch melting experiments.

Data availability

Processed tomographic, mineralogical, and geochemical data generated in this study have been deposited in the University of Arizona ReDATA database [https://doi.org/10.25422/azu.data.25665234].

References

1. T. J. McCoy, D. W. Mittlefehldt, L. Wilson, "Asteroid Differentiation" in *Meteorites and the Early Solar System II*, D. S. Lauretta, H. Y. McSween, Eds. (2006), p. 733.
2. Wang, L. & Fei, Y. A partially equilibrated initial mantle and core indicated by stress-induced percolative core formation through a bridgmanite matrix. *Sci. Adv.* **9**, eade3010 (2023).
3. Gaetani, G. A. & Grove, T. L. Wetting of mantle olivine by sulfide melt: implications for Re/Os ratios in mantle peridotite and late-stage core formation. *Earth Planet. Sci. Lett.* **169**, 147–163 (1999).
4. Crossley, S. D., Ash, R. D., Sunshine, J. M., Corrigan, C. M. & McCoy, T. J. Parent body histories recorded in Rumuruti chondrite sulfides: Implications for the onset of oxidized, sulfur-rich core formation. *Meteorit. Planet. Sci.* **58**, 383–404 (2023).
5. Terasaki, H., Frost, D. J., Rubie, D. C. & Langenhorst, F. The effect of oxygen and sulphur on the dihedral angle between Fe–O–S melt and silicate minerals at high pressure: Implications for Martian core formation. *Earth Planet. Sci. Lett.* **232**, 379–392 (2005).
6. Terasaki, H., Frost, D. J., Rubie, D. C. & Langenhorst, F. Percolative core formation in planetesimals. *Earth Planet. Sci. Lett.* **273**, 132–137 (2008).
7. Rose, L. A. & Brenan, J. M. Wetting Properties of Fe-Ni-Co-Cu-O-S Melts against Olivine: Implications for Sulfide Melt Mobility. *Econ. Geol.* **96**, 145–157 (2001).
8. Yoshino, T., Walter, M. J. & Katsura, T. Core formation in planetesimals triggered by permeable flow. *Nature* **422**, 154–157 (2003).
9. Watson, H. C. & Roberts, J. J. Connectivity of core forming melts: Experimental constraints from electrical conductivity and X-ray tomography. *Phys. Earth Planet. Inter.* **186**, 172–182 (2011).
10. Ghanbarzadeh, S., Hesse, M. A. & Prodanović, M. Percolative core formation in planetesimals enabled by hysteresis in metal connectivity. *Proc. Natl Acad. Sci.* **114**, 13406–13411 (2017).
11. Néri, A. et al. Reevaluation of metal interconnectivity in a partially molten silicate matrix using 3D microtomography. *Phys. Earth Planet. Inter.* **308**, 106571 (2020).
12. Wang, Z., Yao, Z.-S., Jin, Z. & Wang, Y. Experimental Investigation on the Transport of Sulfide Driven by Melt-Rock Reaction in Partially Molten Peridotite. *J. Geophys. Res.: Solid Earth* **128**, e2022JB026065 (2023).
13. McCanta, M. C. et al. The LaPaz Icefield 04840 meteorite: Mineralogy, metamorphism, and origin of an amphibole- and biotite-bearing R chondrite. *Geochim. et. Cosmochim. Acta* **72**, 5757–5780 (2008).
14. Righter, K., Sutton, S. R., Danielson, L., Pando, K. & Newville, M. Redox variations in the inner solar system with new constraints from vanadium XANES in spinels. *Am. Mineral.* **101**, 1928–1942 (2016).
15. Sugaki, A. & Kitakaze, A. High form of pentlandite and its thermal stability. *Am. Miner.* **83**, 133–140 (1998).
16. Raghavan, V. Fe-Ni-S (iron-nickel-sulfur). *J. Phase Equilibria Diffus.* **25**, 373–381 (2004).
17. Tomkins, G., Johnson, T. E. & Mitchell, J. T. A review of the chondrite–achondrite transition, and a metamorphic facies series for equilibrated primitive stony meteorites. *Meteorit. Planet Sci.* **55**, 857–885 (2020).
18. von Bargen, N. & Waff, H. S. Permeabilities, interfacial areas and curvatures of partially molten systems: Results of numerical computations of equilibrium microstructures. *J. Geophys. Res.: Solid Earth* **91**, 9261–9276 (1986).
19. Walker, R. Siderophile Elements in Tracing Planetary Formation and Evolution. *Geochem. Persp.* **5**, 1–145 (2016).
20. Fleet, M. E. & Stone, W. E. Partitioning of platinum-group elements in the Fe-Ni-S system and their fractionation in nature. *Geochim. et. Cosmochim. Acta* **55**, 245–253 (1991).
21. Schrader, D. L., Davidson, J. & McCoy, T. J. Widespread evidence for high-temperature formation of pentlandite in chondrites. *Geochim. et. Cosmochim. Acta* **189**, 359–376 (2016).
22. Schrader, D. L. et al. The Fe/S ratio of pyrrhotite group sulfides in chondrites: An indicator of oxidation and implications for return samples from asteroids Ryugu and Bennu. *Geochim. et. Cosmochim. Acta* **303**, 66–91 (2021).

23. Mungall, J. & Su, S. Interfacial tension between magmatic sulfide and silicate liquids: Constraints on kinetics of sulfide liquation and sulfide migration through silicate rocks. *Earth Planet. Sci. Lett.* **234**, 135–149 (2005).
24. Solferino, G. F. D., Thomson, P.-R. & Hier-Majumder, S. Pore Network Modeling of Core Forming Melts in Planetesimals. *Front. Earth Sci.* **8**, 339 (2020).
25. Bischoff, N. & Vogel, J. Roszjar, The Rumuruti chondrite group. *Geochemistry* **71**, 101–133 (2011).
26. Crossley, S. D. et al. Sulfide-dominated partial melting pathways in brachinites. *Meteorit. Planet Sci.* **55**, 2021–2043 (2020).
27. Day, J. M. D. et al. Origin of felsic achondrites Graves Nunataks 06128 and 06129, and ultramafic brachinites and brachinite-like achondrites by partial melting of volatile-rich primitive parent bodies. *Geochim. et. Cosmochim. Acta* **81**, 94–128 (2012).
28. Nicklas, R. W. et al. Highly siderophile element fractionation during chondrite melting inferred from olivine-rich primitive achondrites. *Geochim. et. Cosmochim. Acta* **351**, 66–77 (2023).
29. Gardner-Vandy, K. G., Lauretta, D. S. & McCoy, T. J. A petrologic, thermodynamic and experimental study of brachinites: Partial melt residues of an R chondrite-like precursor. *Geochim. et. Cosmochim. Acta* **122**, 36–57 (2013).
30. McSween, H. Y. et al. Thermal Evolution Models of Asteroids. in *Asteroids III* (eds. Bottke, W. F., Cellino, A., Paolicchi, P. & Binzel, R. P.) 559–572, University of Arizona Press (2002).
31. Sahijpal, S., Soni, P. & Gupta, G. Numerical simulations of the differentiation of accreting planetesimals with ^{26}Al and ^{60}Fe as the heat sources. *Meteorit. Planet. Sci.* **42**, 1529–1548 (2007).
32. Sugiura, N. & Fujiya, W. Correlated accretion ages and ε^{54}Cr of meteorite parent bodies and the evolution of the solar nebula. *Meteorit. Planet. Sci.* **49**, 772–787 (2014).
33. Keil, K. Brachinite meteorites: Partial melt residues from an FeO-rich asteroid. *Geochemistry* **74**, 311–329 (2014).
34. Edwards, G. H. & Blackburn, T. Accretion of a large LL parent planetesimal from a recently formed chondrule population. *Sci. Adv.* b, eaay8641 (2020).
35. Maurel, J. F. J. et al. Weiss, Meteorite evidence for partial differentiation and protracted accretion of planetesimals. *Sci. Adv.* **6**, eaba1303 (2020).
36. Kitakaze, T. & Machida, R. Komatsu, Phase Relations In the Fe–Ni–s System From 875 To 650 °C. *Can. Miner.* **54**, 1175–1186 (2016).
37. Waldner, P. & Pelton, A. D. Critical thermodynamic assessment and modeling of the Fe-Ni-S system. *Met. Mater. Trans. B* **35**, 897–907 (2004).
38. Hauck, S. A. Sulfur's impact on core evolution and magnetic field generation on Ganymede. *J. Geophys. Res.: Planets* **111**, E09008 (2006). I. I., J. M. Aurnou, A. J. Dombard.
39. Kracher, J. Willis, Composition and Origin of the Unusual Oktibbeha County Iron Meteorite. *Meteoritics* **16**, 239–246 (1981).
40. Warren, P. H. Stable-isotopic anomalies and the accretionary assemblage of the Earth and Mars: A subordinate role for carbonaceous chondrites. *Earth Planet. Sci. Lett.* **311**, 93–100 (2011).
41. Nanne, J. A. M., Nimmo, F., Cuzzi, J. N. & Kleine, T. Origin of the non-carbonaceous–carbonaceous meteorite dichotomy. *Earth Planet. Sci. Lett.* **511**, 44–54 (2019).
42. Suttle, M. D. et al. The mineralogy and alteration history of the Yamato-type (CY) carbonaceous chondrites. *Geochim. et. Cosmochim.Acta* **361**, 245–264 (2023).
43. Bryson, J. F. J. et al. Paleomagnetic Evidence for a Partially Differentiated Ordinary Chondrite Parent Asteroid. *J. Geophys. Res.: Planets* **124**, 1880–1898 (2019).
44. Cournède, J., Gattacceca, P., Rochette, D. L. & Shuster Paleomagnetism of Rumuruti chondrites suggests a partially differentiated parent body. *Earth Planet. Sci. Lett.* **533**, 116042 (2020).
45. Righter, K. & Neff, K. E. Temperature and oxygen fugacity constraints on CK and R chondrites and implications for water and oxidation in the early solar system. *Polar Sci.* **1**, 25–44 (2007).
46. Walte, N. P., Solferino, G. F. D., Golabek, G. J., Silva Souza, D. & Bouvier, A. Two-stage formation of pallasites and the evolution of their parent bodies revealed by deformation experiments. *Earth Planet. Sci. Lett.* **546**, 116419 (2020).
47. Zimmerman, M. E. & Kohlstedt, D. L. Rheological Properties of Partially Molten Lherzolite. *J. Petrol.* **45**, 275–298 (2004).
48. Iida, T. & Guthrie, R. I. L. *The Thermophysical Properties of Metallic Liquids*. First edition (Oxford University Press, United Kingdom, 2015).
49. Shannon, M. C. & Agee, C. B. Percolation of core melts at lower mantle conditions. *Science* **280**, 1059–1061 (1998).
50. Schmidt, M. E., Schrader, C. M. & McCoy, T. J. The primary fO_2 of basalts examined by the Spirit rover in Gusev Crater, Mars: Evidence for multiple redox states in the martian interior. *Earth Planet. Sci. Lett.* **384**, 198–208 (2013).
51. Righter, K. & Chabot, N. L. Moderately and slightly siderophile element constraints on the depth and extent of melting in early Mars. *Meteorit. Planet. Scien* **46**, 157–176 (2011).
52. Rai, N. & van Westrenen, W. Core-mantle differentiation in Mars. *J. Geophys. Res.: Planets* **118**, 1195–1203 (2013).
53. Yang, S. et al. Siderophile and chalcophile element abundances in shergottites: Implications for Martian core formation. *Meteorit. Planet. Scien* **50**, 691–714 (2015).
54. Stähler, S. C. et al. Seismic detection of the martian core. *Science* **373**, 443–448 (2021).
55. Irving, J. C. E. et al. First observations of core-transiting seismic phases on Mars. *Proc. Natl Acad. Sci.* **120**, e2217090120 (2023).
56. Khan, D., Huang, C., Durán, P. A., Sossi, D. & Giardini, M. Murakami, Evidence for a liquid silicate layer atop the Martian core. *Nature* **622**, 718–723 (2023).
57. Greenwood, J. P., Rubin, A. E. & Wasson, J. T. Oxygen isotopes in R-chondrite magnetite and olivine: links between R chondrites and ordinary chondrites. *Geochim. et. Cosmochim. Acta* **64**, 3897–3911 (2000).
58. Terasaki, H. Pressure and Composition Effects on Sound Velocity and Density of Core-Forming Liquids: Implication to Core Compositions of Terrestrial Planets. *J. Geophys. Res.: Planets* **124**, 2272–2293 (2019).
59. Day, J. M. D., Brandon, A. D. & Walker, R. J. Highly Siderophile Elements in Earth, Mars, the Moon, and Asteroids. *Rev. Mineral. Geochem.* **81**, 161–238 (2016).
60. Kleine, T. et al. Hf–W chronology of the accretion and early evolution of asteroids and terrestrial planets. *Geochim. et. Cosmochim. Acta* **73**, 5150–5188 (2009).
61. Marchi, S., Walker, R. J. & Canup, R. M. A compositionally heterogeneous martian mantle due to late accretion. *Sci. Adv.* **6**, eaay2338 (2020).
62. O'Neill, H. S. C. & Pownceby, M. I. Thermodynamic data from redox reactions at high temperatures. I. An experimental and theoretical assessment of the electrochemical method using stabilized zirconia electrolytes, with revised values for the Fe-"FeO", Co-CoO, Ni-NiO and Cu-Cu2O oxygen buffers, and new data for the W-WO2 buffer. *Contr. Mineral. Petrol.* **114**, 296–314 (1993).
63. Righter, K., Hervig, R. L. & Kring, D. A. Accretion and core formation on Mars: molybdenum contents of melt inclusion glasses in three SNC meteorites. *Geochim. et. Cosmochim. Acta* **62**, 2167–2177 (1998).
64. Righter, K. & Shearer, C. K. Magmatic fractionation of Hf and W: constraints on the timing of core formation and differentiation in the Moon and Mars. *Geochim. et. Cosmochim. Acta* **67**, 2497–2507 (2003).
65. Kruijer, T. S. et al. The early differentiation of Mars inferred from Hf–W chronometry. *Earth Planet. Sci. Lett.* **474**, 345–354 (2017).

66. Connolly, H. C. et al. *The Meteoritical Bulletin*, No. **91** (2007).
67. Wohlgemuth-Ueberwasser, C. C. et al. Synthesis of PGE sulfide standards for laser ablation inductively coupled plasma mass spectrometry (LA-ICP-MS). *Contrib. Miner. Pet.* **154**, 607–617 (2007).
68. Konkena, B. et al. Pentlandite rocks as sustainable and stable efficient electrocatalysts for hydrogen generation. *Nat. Commun.* **7**, 12269 (2016).
69. Walker, R. J. et al. Modeling fractional crystallization of group IVB iron meteorites. *Geochim. et. Cosmochim. Acta* **72**, 2198–2216 (2008).
70. Paul, B. et al. Time resolved trace element calibration strategies for LA-ICP-MS. *J. Anal. Spectrom.* **38**, 1995–2006 (2023).
71. Howell, D., Griffin, W. L., Pearson, N. J., Powell, W. & O'Reilly, S. Y. Trace element partitioning in mixed-habit diamonds. *Chem. Geol.* **355**, 134–143 (2013).
72. Lanari, P., Vho, A., Bovay, T., Airaghi, L. & Centrella, S. Quantitative compositional mapping of mineral phases by electron probe micro-analyser. *SP* **478**, 39–63 (2019).
73. Lanari, P. et al. XMapTools: A MATLAB©-based program for electron microprobe X-ray image processing and geothermobarometry. *Comput. Geosci.* **62**, 227–240 (2014).
74. Ludwig, K. R. User's manual for Isoplot 3.00: a geochronological toolkit for Microsoft Excel. *Berkeley Geochronology Center Special Publication* (2003).
75. Ketcham, R. A. & Carlson, W. D. Acquisition, optimization and interpretation of X-ray computed tomographic imagery: applications to the geosciences. *Comput. Geosci.* **27**, 381–400 (2001).
76. Hanna, R. D. & Ketcham, R. A. Evidence for accretion of fine-grained rims in a turbulent nebula for CM Murchison. *Earth Planet. Sci. Lett.* **481**, 201–211 (2018).
77. Helmy, H. M. & Bragagni, A. Platinum-group elements fractionation by selective complexing, the Os, Ir, Ru, Rh-arsenide-sulfide systems above 1020 °C. *Geochim. et. Cosmochim. Acta* **216**, 169–183 (2017).
78. McDonough, W. F. & Sun, S.-s The composition of the Earth. *Chem. Geol.* **120**, 223–253 (1995).

Acknowledgements

The authors would like to acknowledge contributions from K. Prissel, G. Moore, and F. McCubbin, whose thoughtful discussions and technical recommendations to S.D.C. throughout experiments were pivotal to the success of this work. We would also like to thank J. Gorce for assistance with electron microprobe analyses at ARES. Support for S.D.C was provided by the Gordon A. McKay Postdoctoral Fellowship in Petrology and Geochemistry at ARES NASA JSC and LPI. NASA Planetary Science funding from the ISFM Program supported research activities at NASA Johnson Space Center. We also acknowledge support from the JETSII contract (#80JSC022DA035: J.B.S., B.A.A., K.I., W.P.B., S.A.E., and E.W.O.) at NASA Johnson Space Center. Access to the LPI SEM Facility and UTCT instrumentation was provided in part by the NASA PSEF program (80NSSC23K0197 and 80NSSC23K0199, respectively).

Author contributions

S.D.C. led initial conceptualization, conducted melting experiments and in situ analyses, interpreted data, created figures, and led writing for the original and revised drafts. J.B.S. developed methodology for in situ trace element analysis, processed trace element data, and contributed writing and revisions for relevant sections. B.A.A. and K.I. contributed to experimental methods development and writing revisions. W.P.B. developed and undertook wet chemistry methods for trace element dopants in synthetic experiments. S.A.E. and E.W.O. collected whole rock μXCT scans of meteorite partial melting experiments, processed tomography data, developed dimensional analysis methods, and contributed to writing relevant sections. J.A.M. conducted high resolution μXCT of the experimental subvolume and processed tomography data. J.I.S. contributed to trace element geochemical methodology and supervision of the lead author. K.R. contributed to the development of experimental methods, as well as supervision of the lead author.

Competing interests

The authors declare no competing interests.

Additional information

Supplementary information The online version contains supplementary material available at https://doi.org/10.1038/s41467-025-58517-8.

Correspondence and requests for materials should be addressed to Samuel D. Crossley.

Peer review information *Nature Communications* thanks Lin Wang, and the other, anonymous, reviewer(s) for their contribution to the peer review of this work. A peer review file is available.